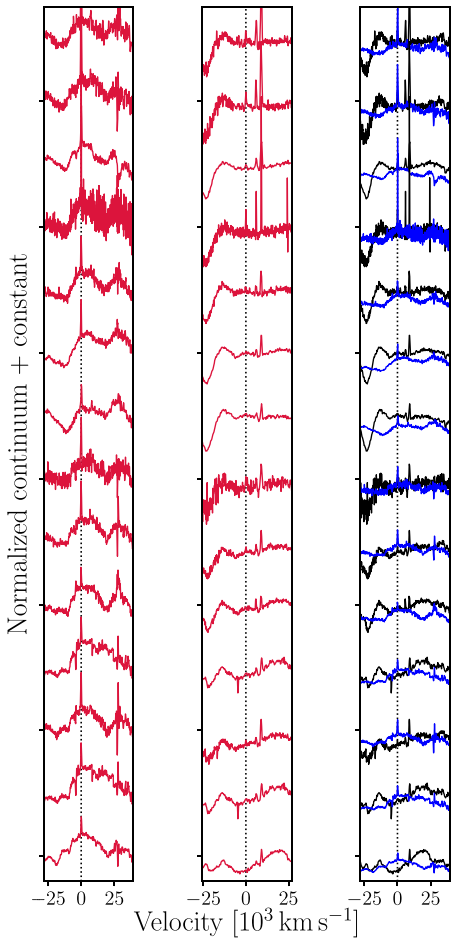

Figure 13. Left-hand panel: a close-up of the H α region in the early spectral evolution of SN 2018hti (red solid lines). Central panel: same as in the left-hand panel, but for the H β region. Right-hand panel: overlap of the H α (blue solid lines) and H β (black solid lines) regions, where the H α region was superposed on that of H β. The dotted vertical black lines mark the rest-frame wavelength of H β (middle panel) and of H α (left- and right-hand panel). The rest-frame phases of the spectra are labelled on the right side of the right-hand panel.

in SLSNe I (see Section 4.5.3) as a guide for the interpretation of the pseudo-nebular spectrum of SN 2018hti. This allows us to constrain the mass of the progenitor of SN 2018hti.

4.5.1 The early boxy feature

The flat-topped line profile of the emission feature at ∼6500 Å could be suitably explained by emission inside an expanding shell of matter (Weiler 2003; Jerkstrand 2017).The identification of this feature is not straightforward, and could be attributed either to H α or to C II λ 6580. To investigate this line identification, we superimpose on top of the boxy feature the line profiles of the possible H β (where a tiny bump is present, see Fig. 13) and of C II λ 9234 (see Fig. 14). The comparison between the H α and H β spectral regions is arduous because the H β region is also potentially contaminated by other spectral features (such as O II and Fe II). On the other hand, the boxy line is well reproduced by the C II λ 9234 feature in the IRTF+SpeX spectrum, suggesting that their flat profiles stem from the same matter

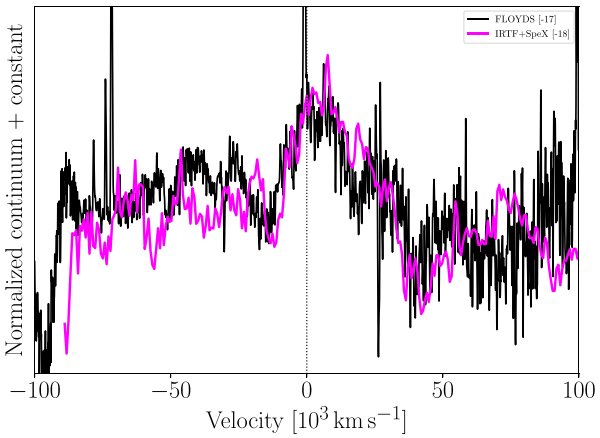

Figure 14. Comparison between the continuum-normalized FLOYDS (black line) and IRTF+SpeX (magenta line) spectra of SN 2018hti at comparable phases. The optical and the NIR spectra are plotted in velocity coordinates with respect to $\lambda = 6580$ Å and $\lambda = 9234$ Å, respectively.

shell and thus favouring a C II λ 6580 identification. Detailed radiative transfer calculations (e.g. Dessart et al. 2012; Dessart 2019) actually predict the presence of the C II λ 6580 feature in the SLSNe I spectra, but do not predict the boxy shape for the C II λ 6580. This suggests that the models may need to more carefully account for dynamical effects such as the formation of a thick shell, which is expected from both from magnetar and CSM interaction scenario.

4.5.2 Light curves fits with MOSFIT

MOSFIT includes a number of models for different kinds of astronomical transients. In particular, those suitable for the SLSNe I are the CSM (CSM interaction powered), CSMNI (CSM interaction $+^{56}$Ni-decay powered), the SLSN and the MAGNETAR (two implementations of the magnetar powered case, see later), and the MAGNI (magnetar+^{56}Ni-decay powered) models. We chose the SLSN and the CSM modules to fit the photometry of SN 2018hti, which, respectively, exploit the models introduced by Inserra et al. (2013) and Chatzopoulos, Wheeler & Vinko (2012). Since MOSFIT takes as input the multiband LCs, it has to rebuild the pseudo-bolometric luminosities once an SED model has been assumed. We chose the SLSN model since it accounts for the UV blanketing assuming an absorbed-blackbody model for the SED computation. We excluded the $W1$, $W2$ magnitudes from the fit procedure since the MIR part of the SED could deviate from a single blackbody component at epochs which are not covered by our photometric data set.

Also, the SLSN model includes constraints ensuring the energy conservation and that the ejecta do not become optically thin before 100 d after maximum, as not to contradict the late spectroscopic observations of the SLSNe (see section 3.8 in Nicholl et al. 2017b). The results of the fit procedures are shown in Figs 15 and 16 and the corner plots are shown in Figs S1 and S2 (available as online supplementary material). The SLSN fit supports a magnetar engine with a polar magnetic field of $\sim 1.3 \times 10^{13}$ G and an initial period of ∼1.8 ms, for an ejecta mass $M_{\rm ejecta} \approx 5.3\,{\rm M}_{\odot}$, opacity $\kappa \approx 0.1\,{\rm cm^2\,g^{-1}}$, gamma-ray opacity $\kappa_{\gamma} \approx 0.02\,{\rm cm^2\,g^{-1}}$, an average ejecta velocity $v_{\rm ej} \approx 8500\,{\rm km\,s^{-1}}$, and a temperature floor $T_{\rm min} \approx 9300 \pm 250$ K. This corresponds to a kinetic energy $E_{\rm kin} = 3.7 \times 10^{51}$ erg. These results are absolutely reasonable for what is expected by the magnetar scenario for SLSNe I (e.g. Nicholl

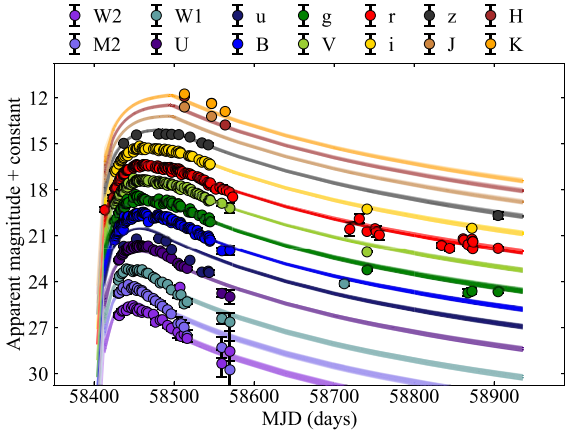

Figure 15. Best-fitting MOSFIT synthetic LCs to the multiband photometry of SN 2018hti obtained with the SLSN model.

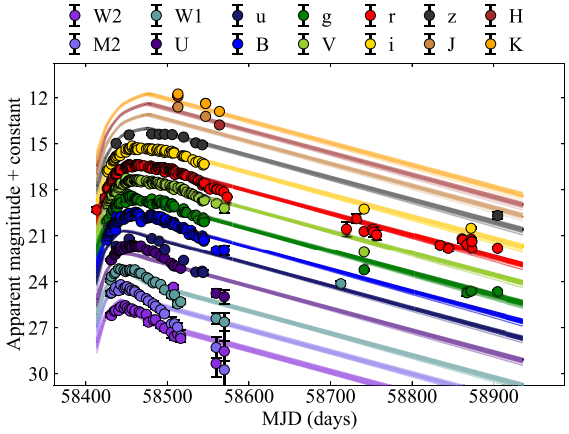

Figure 16. Same as in Fig. 15, but for the CSM model.

et al. 2017b) and are in perfect agreement with the estimates of Lin et al. (2020a). Except for the ejecta mass, the best-fitting parameters for the magnetar case are quite different from those assumed in the calculations of Kasen & Bildsten (2010). This difference could possibly explain the need of the scaling factor 1.37 that we used in Section 4.3 to match the predicted photospheric velocity with the observed one. Moreover, the value of the kinetic energies required by both interpretations largely overcomes the maximum explosion energy that can be provided by a neutrino-driven mechanism during the core collapse (Soker & Gilkis 2017; Kaplan & Soker 2020). This energy budget might require the contribution of jets in the explosion of SN 2018hti. However, its negligible polarization degree (Lee 2019) suggests that its explosion was nearly spherical, thus making this hypothesis less likely.

The CSM fit of SN 2018hti instead requires the interaction of the SN ejecta with a mass of $\sim 8.3\,M_\odot$ and average velocity $v_{ej} \approx 1.1 \times 10^4\,km\,s^{-1}$ with a CSM mass $M_{CSM} \approx 10.5\,M_\odot$ and average density $\rho \approx 4.1 \times 10^{-13}\,g\,cm^{-3}$. This corresponds to a kinetic energy $E_{kin} = 1.1 \times 10^{52}$ erg. Also, for this model the predicted temperature floor reached by SN 2018hti is $T_{min} \approx 9500 \pm 180$ K. Both the predictions of T_{min} can be considered in agreement with what was deduced in Section 4.2. The best-fitting slope of the CSM density profile $s \sim 0.2$ seemingly favours a shell-like CSM with nearly constant density (Chatzopoulos et al. 2013). The CSM interaction scenario may be disfavoured because of the absence of narrow/multicomponent features in the spectra (typical e.g. of SNe IIn) and because there was no significant detection in X-ray (see Section 2). However, these arguments cannot rule out the CSM-interaction scenario for SN 2018hti if the CSM is highly asymmetric, e.g. if it has a disc-like geometry. In fact, if the CSM is not seen perfectly edge on, the optically thick ejecta may form a photosphere outside the CSM so that the ejecta CSM interaction takes place underneath it and the X-ray, UV photons can be reprocessed by further radiation–matter interactions (as it was proposed by Andrews & Smith 2018, for the peculiar SN II iPTF14hls).

4.5.3 *Interpretation of the nebular spectrum*

The nebular spectrum of SN 2018hti taken 269 rest-frame days after maximum light was interpreted with SUMO modelling (Jerkstrand et al. 2017).The best-matching SUMO models are built with a C-burning composition, $M_{ejecta} = 30\,M_\odot$, a filling factor $f = 0.001$, an energy deposition $E_{dep} = 10^{42}\,erg\,s^{-1}$ and a pure-O abundance $M_{ejecta} = 10\,M_\odot$, $f = 0.1$, $E_{dep} = 2 \times 10^{42}\,erg\,s^{-1}$. In the following text, we will refer to them as C30 and O10, respectively. They are shown in Fig. 17 with the pseudo-nebular spectrum of SN 2018hti. In particular, O10 better reproduces the bluer region of the spectrum (until ∼5200 Å, see Fig. 17), whereas C30 better matches the redder region. Also, the best-matching spectra permit identification of other broad features in the spectrum, such as [O III] λλ 4959, 5007, Mg I λ 5180+[Fe II] λ 5250, and [O I] λ 5577. We estimated the progenitor mass of SN 2018hti by measuring the flux emitted within the O I λ 7774 emission feature predicted by C30 using equations (7) and (8) of Jerkstrand et al. (2017). The choice of C30 is motivated by the fact that it better describes the Oxygen features in the spectrum, as the [O I] λλ 6300, 6364 and [O I] λ 5577 features. The flux integrated within the O I λ 7774 feature gives $L_{7774} = 2.25 \times 10^{40}\,erg\,s^{-1}$. Hence, we assumed $f = 0.001$, the Oxygen mean molecular weight $\bar{A} = 16$, an electron fraction $x_e = 0.1$ (Jerkstrand et al. 2017, see their section 4.2.1), a maximum expansion velocity $V = 8\,000\,km\,s^{-1}$ (we adopted for V a value consistent with the velocity plateau at late times, see Fig. 10), and a recombination coefficient $\alpha^{eff}(T) = 2 \times 10^{-13}\,cm^3\,s^{-1}$. Solving equation (7) of Jerkstrand et al. (2017) for the electron density n_e, this gives $n_e \sim 1.28 \times 10^9\,cm^{-3}$. Using this value in equation (8) in Jerkstrand et al. (2017), the O-zone mass is estimated to be $M_{O-zone} \approx 6.2\,M_\odot$, which according to more recent models of stellar evolution of a single star corresponds to a progenitor mass $M_{ZAMS} \approx 40\,M_\odot$ (Jerkstrand et al. 2017). Similar consideration can be made for the O10 solution (corresponding to $f = 0.1$ and $x_e \approx 0.5$), which predicts a O-zone mass $M_{O-zone} \approx 10\,M_\odot$ (for this solution we require $V \lesssim 7\,000\,km\,s^{-1}$ in order not to obtain $M_{O\text{-zone}} > M_{ejecta}$). In the latter case, the ejecta is expected to be much Mg-poorer compared to the C30 case. Another reason to favour the C30 model lies in its ejecta clump density. In fact, C30 is 300 times denser than O10.[13] This could be also the reason why no strong [O I]λ 6300 and [Ca II] + [O II] λ 7300 emission is seen in the nebular spectrum, as it would emerge for higher density models.

Finally, in Table 3 we summarized the ejecta-mass estimates obtained with the MOSFIT fits and the SUMO nebular modelling. The SUMO O10 solution apparently favours the CSM model since the

[13]The factor 300 comes from $(30\,M_\odot/f_{C30})/(10\,M_\odot/f_{O10}) = 300$, where $f_{C30} = 0.001$ and $f_{O10} = 0.1$ are the clumping factors for the models C30 and O10, respectively.

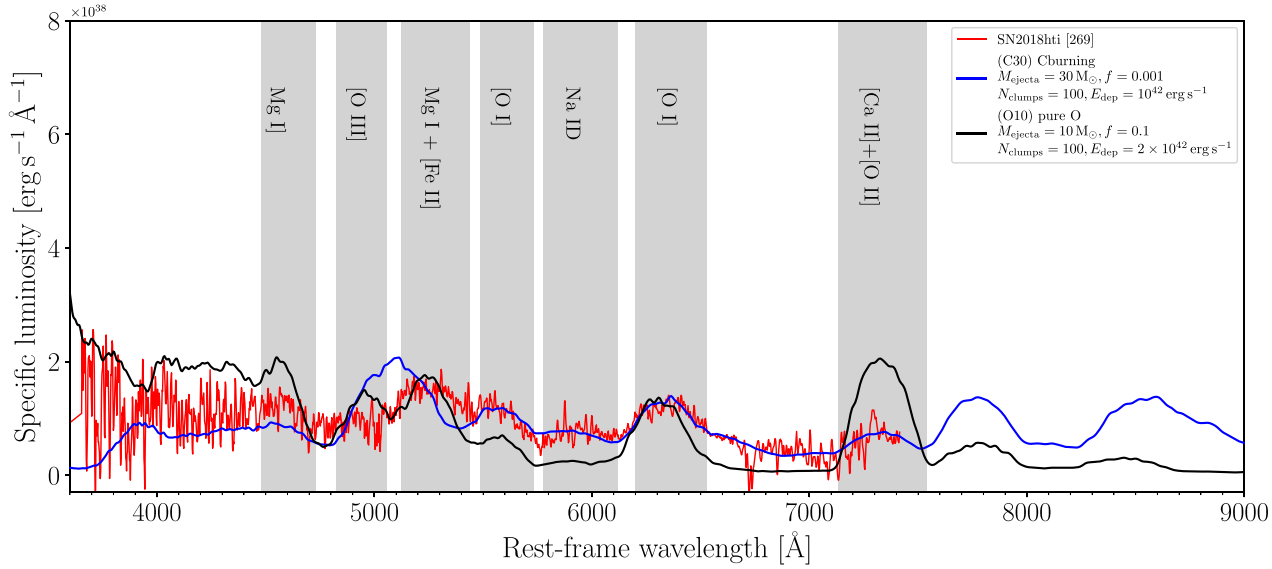

Figure 17. Comparison of the GTC+OSIRIS nebular spectrum (red line) with two outputs of the SUMO numerical code (see the text) for a full C-ashes model (blue line) and a pure-O composition (black line).

Table 3. Comparison of the ejecta masses of the best-matching SUMO solutions with MOSFIT best-fitting parameters.

	Ejecta mass [$M_\odot$]
SUMO	10–30
MOSFIT CSM	8.32
MOSFIT SLSN	5.25

ejecta mass used by O10 nearly reproduces that one estimated by the MOSFIT CSM fit, whereas the MOSFIT SLSN fit predicts an ejecta mass which is pretty lower than what is suggested by the SUMO solutions. However, we warn the reader that the (single-zone) SUMO solutions are computed for a phase of 400 d post-explosion, which is not the case for the pseudo-nebular spectrum of SN 2018hti. Hence, the density in the model is by a factor $(400/270)^3 \simeq 3.3$ lower than the corresponding case at 270 d. This biases a direct constrain on the ejecta density and mass. In addition, it is hard to believe that in the case of SN 2018hti the CSM interaction is acting as its major power source even if we interpret the modest C II boxy feature as a signature of the interaction with a CSM dense shell. According to the MOSFIT CSM fit, the predicted CSM mass is $\sim$10.5 $M_\odot$. We expect that the interaction with a similar amount of mass of CSM would cause strong spectral emissions as in the case of the Type IIn SN 2008iy (Chugai 2021) and SN 2010jl (Ofek et al. 2014). However, as we mentioned earlier, a disc-like and dense CSM can hide the spectral signatures of CSM-interaction. Based on this considerations, we argue that the mechanism powering SN 2018hti could be either the spin-down radiation from a millisecond magnetar with $B_p \sim 1.3 \times 10^{13}$ G and $P_{spin} \sim 1.8$ ms or the (buried) interaction of the ejecta with $\sim$10 $M_\odot$ of a disc-like CSM.

5 CONCLUSIONS

In this work, we have presented the UV/optical/NIR photometry and the NIR/optical spectroscopy of the SLSN I SN 2018hti. It slowly rose for $\sim$50 d towards a peak absolute magnitude of -21.7 mag in the r band. Alongside this slow rise and extremely high luminosity, the presence of the prominent O II absorptions in the pre-maximum/maximum spectra identifies this object as a (slow-evolving) SLSN I. In the Hα region, the early spectra show a flat-topped feature which we interpret as Hα. C-rich SLSNe I spectra are predicted by magnetar- and a pair-instability-driven radiative transfer calculations (Dessart et al. 2012; Dessart 2019), but the boxy profile suggests that the feature could originate from the shock-mediated interaction of the SN ejecta with a surrounding CSM. In addition, metallicity measurements via the host narrow emission lines are aligned with the low-metallicity paradigm of SLSNe I. Finally, we estimated the physical parameters of the explosion, both in the magnetar and in the CSM-interaction scenarios, fitting synthetic LCs to the multicolour photometry of SN 2018hti with the MOSFIT tool. The model fits suggest that either interaction of a 8 $M_\odot$ SN ejecta with $\sim$10 $M_\odot$ of CSM or the spin-down radiation of a $B \sim 1.3 \times 10^{13}$ G, $P_{spin} \sim 1.8$ ms magnetar could be the major power source for SN 2018hti.

We interpret the pseudo-nebular spectrum of SN 2018hti with synthetic spectra published by Jerkstrand et al. (2017) for an SN Ic. We concluded that, assuming a single-star progenitor scenario for SN 2018hti, the progenitor ZAMS mass was of $\sim$40 $M_\odot$. These findings help to unravel the origin of the complexities that often appear in SLSNe-I LCs (e.g. Inserra et al. 2017), finding a reasonable explanation in CSM-ejecta interaction. This sheds light on the nature of SLSNe I progenitors.

The advent of the new-generation, wide-field surveys such as the Legacy Survey of Space and Time at the Vera Rubin Observatory will contribute to broaden our knowledge about the SLSN astrophysics (Villar, Nicholl & Berger 2018).

ACKNOWLEDGEMENTS

We thank the anonymous referee for her/his valuable comments which improved the present work. AF acknowledges Stephen Smarrt, Marica Branchesi, Noam Soker, and Morgan Fraser for their sug-

gestions and for interesting discussions. This work is based on observations made with the Nordic Optical Telescope, owned in collaboration by the University of Turku and Aarhus University, and operated jointly by Aarhus University, the University of Turku and the University of Oslo, representing Denmark, Finland and Norway, the University of Iceland and Stockholm University at the Observatorio del Roque de los Muchachos, La Palma, Spain, of the Instituto de Astrofisica de Canarias. The data presented here were obtained in part with ALFOSC, which is provided by the Instituto de Astrofisica de Andalucia (IAA) under a joint agreement with the University of Copenhagen and NOT. Based on observations collected at Copernico and Schmidt telescopes (Asiago, Italy) of the INAF - Osservatorio Astronomico di Padova. MG is supported by the EU Horizon 2020 research and innovation programme under grant agreement No 101004719. MS acknowledges the Infrared Telescope Facility, which is operated by the University of Hawaii under contract 80HQTR19D0030 with the National Aeronautics and Space Administration. NER acknowledges support from MIUR, PRIN 2017 (grant 20179ZF5KS). TMB was funded by the CONICYT PFCHA / DOCTORADOBECAS CHILE/2017-72180113. AJ acknowledges funding from the European Research Council (ERC) under the European Union's Horizon 2020 Research and Innovation Program (ERC Starting Grant. AR acknowledges support from ANID BECAS/DOCTORADO NACIONAL 21202412. Y-Z Cai is funded by China Postdoctoral Science Foundation (grant no. 2021M691821). T-WC acknowledges the EU Funding under Marie Skłodowska-Curie grant H2020-MSCA-IF-2018-842471. KM is funded by the EU H2020 ERC grant no. 758638. GP is supported by ANID - Millennium Science Initiative - ICN12_009. We thank the staff at the different observatories for performing the observations. Based on observations collected at the European Organisation for Astronomical Research in the Southern Hemisphere, Chile, as part of ePESSTO+ (the advanced Public ESO Spectroscopic Survey for Transient Objects). ePESSTO+ observations were obtained under ESO program id 199.D-0143 (PI: Inserra). Based on observations made with the Gran Telescopio Canarias (GTC), installed in the Spanish Observatorio del Roque de los Muchachos of the Instituto de Astrofísica de Canarias, in the island of La Palma. This work uses observations from the Las Cumbres Observatory network. The LCO team is supported by NSF grants AST-1911225 and AST-1911151.

DATA AVAILABILITY STATEMENT

The data presented in this paper and listed in Appendix A are available in the online supplementary material. The spectra will be made public via WISEREP.

REFERENCES

(HEASARC) N. H. E. A. S. A. R. C., 2014, Astrophysics Source Code Library, record ascl:1408.004
Agnoletto I. et al., 2009, ApJ, 691, 1348
Anderson J. P. et al., 2018, A&A, 620, A67
Anderson J. P., 2019, A&A, 628, A7
Andrews J. E., Smith N., 2018, MNRAS, 477, 74
Angus C. R. et al., 2019, MNRAS, 487, 2215
Asplund M., Grevesse N., Sauval A. J., Scott P., 2009, ARA&A, 47, 481
Becker A., 2015, Astrophysics Source Code Library, record ascl:1504.004
Bhirombhakdi K., Chornock R., Miller A. A., Filippenko A. V., Cenko S. B., Smith N., 2019, MNRAS, 488, 3783
Bianco F. B., Modjaz M., Oh S. M., Fierroz D., Liu Y. Q., Kewley L., Graur O., 2016, Astron. Comput., 16, 54
Blanchard P. K., Nicholl M., Berger E., Chornock R., Milisavljevic D., Margutti R., Gomez S., 2019, ApJ, 872, 90
Brown T. M. et al., 2013, PASP, 125, 1031
Burke J., Hiramatsu D., Arcavi I., Howell D. A., Mccully C., Valenti S., 2018, Transient Name Server Classification Report, 2018–1719, 1
Cappellaro E., 2014, snoopy: a package for SN photometry, Available at: http://sngroup.oapd.inaf.it/snoopy.html
Cardelli J. A., Clayton G. C., Mathis J. S., 1988, ApJ, 329, L33
Cardelli J. A., Clayton G. C., Mathis J. S., 1989, ApJ, 345, 245
Cepa J. et al., 2000, in Iye M., Moorwood A. F., eds, Proc. SPIE Conf. Ser. Vol. 4008, Optical and IR Telescope Instrumentation and Detectors. SPIE, Bellingham, p. 623
Chambers K. C. et al., 2016, preprint (arXiv:1612.05560)
Chatzopoulos E., Wheeler J. C., Vinko J., 2012, ApJ, 746, 121
Chatzopoulos E., Wheeler J. C., Vinko J., Horvath Z. L., Nagy A., 2013, ApJ, 773, 76
Chen T.-W. et al., 2013, ApJ, 763, L28
Chen K.-J., Woosley S. E., Sukhbold T., 2016, ApJ, 832, 73
Chen T.-W., Smartt S. J., Yates R. M., Nicholl M., Krühler T., Schady P., Dennefeld M., Inserra C., 2017a, MNRAS, 470, 3566
Chen T. W. et al., 2015, MNRAS, 452, 1567
Chen T. W. et al., 2017b, A&A, 602, A9
Chevalier R. A., Fransson C., 2003, Supernova Interaction with a Circumstellar Medium. Springer Berlin Heidelberg, Berlin, Heidelberg, p. 171
Chevalier R. A., Irwin C. M., 2011, ApJ, 729, L6
Chonis T. S., Gaskell C. M., 2008, AJ, 135, 264
Chugai N. N., 2021, MNRAS, 508, 6023
Conley A. et al., 2006, AJ, 132, 1707
Cushing M. C., Vacca W. D., Rayner J. T., 2004, PASP, 116, 362
De Cia A. et al., 2018, ApJ, 860, 100
Denicoló G., Terlevich R., Terlevich E., 2002, MNRAS, 330, 69
Dessart L., 2019, A&A, 621, A141
Dessart L., Hillier D. J., Waldman R., Livne E., Blondin S., 2012, MNRAS, 426, L76
Dessart L., Hillier D. J., Woosley S., Livne E., Waldman R., Yoon S.-C., Langer N., 2015, MNRAS, 453, 2189
Elias-Rosa N. et al., 2006, MNRAS, 369, 1880
Fiore A. et al., 2021, MNRAS, 502, 2120
Gal-Yam A., 2012, Science, 337, 927
Gal-Yam A., 2019a, ARA&A, 57, 305
Gal-Yam A., 2019b, ApJ, 882, 102
Gal-Yam A., Yaron O., Pastorello A., Taubenberger S., Fraser M., Perley D., 2021, Transient Name Server AstroNote, 76, 1
Gehrels N. et al., 2004, ApJ, 611, 1005
Ginzburg S., Balberg S., 2012, ApJ, 757, 178
Gomez S., Berger E., Hosseinzadeh G., Blanchard P. K., Nicholl M., Villar V. A., 2021, ApJ, 913, 143
Groves B., Brinchmann J., Walcher C. J., 2012, MNRAS, 419, 1402
Guillochon J., Nicholl M., Villar V. A., Mockler B., Narayan G., Mandel K. S., Berger E., Williams P. K. G., 2017, Astrophysics Source Code Library, record ascl:1710.006
Guillochon J., Nicholl M., Villar V. A., Mockler B., Narayan G., Mandel K. S., Berger E., Williams P. K. G., 2018, ApJS, 236, 6
Harris J., Zaritsky D., 2009, AJ, 138, 1243
Harutyunyan A. H. et al., 2008, A&A, 488, 383
Heger A., Woosley S. E., 2002, ApJ, 567, 532
Holmbo S. et al., 2019, The Astronomer's Telegram, 12661, 1
Hosseinzadeh G., Berger E., Metzger B. D., Gomez S., Nicholl M., Blanchard P., 2021, preprint (arXiv:2109.09743)
Howell D. A., 2017, Superluminous Supernovae. Springer International Publishing, Cham, p. 431
Inserra C. et al., 2013, ApJ, 770, 128
Inserra C. et al., 2017, MNRAS, 468, 4642
Inserra C., 2019, Nat. Astron., 3, 697
Jeffery D. J., Branch D., 1990, in Wheeler J. C., Piran T., Weinberg S., eds, Jerusalem Winter School for Theoretical Physics Vol. 6, Supernovae. World Scientific Publishing Co., Singapore, p. 149
Jerkstrand A. et al., 2017, ApJ, 835, 13

Jerkstrand A., 2017, Spectra of Supernovae in the Nebular Phase. Springer International Publishing, Cham, p. 795
Kangas T. et al., 2017, MNRAS, 469, 1246
Kaplan N., Soker N., 2020, MNRAS, 492, 3013
Kasen D., Bildsten L., 2010, ApJ, 717, 245
Kasen D., Woosley S. E., Heger A., 2011, ApJ, 734, 102
Kennicutt Robert C. J., 1998, ARA&A, 36, 189
Kewley L. J., Dopita M. A., 2002, ApJS, 142, 35
Kewley L. J., Ellison S. L., 2008, ApJ, 681, 1183
Khetan N. et al., 2021, A&A, 647, A72
Könyves-Tóth R., Vinkó J., 2021, ApJ, 909, 24
Lee C.-H., 2019, ApJ, 875, 121
Leloudas G. et al., 2012, A&A, 541, A129
Leloudas G. et al., 2015, MNRAS, 449, 917
Lin W. L. et al., 2020a, MNRAS, 497, 318
Lin W. L., Wang X. F., Wang L. J., Dai Z. G., 2020b, ApJ, 903, L24
Lunnan R. et al., 2014, ApJ, 787, 138
Lunnan R. et al., 2018a, Nat. Astron., 2, 887
Lunnan R. et al., 2018b, ApJ, 852, 81
Lunnan R. et al., 2020, ApJ, 901, 61
Maiolino R. et al., 2008, A&A, 488, 463
Margalit B., Metzger B. D., Thompson T. A., Nicholl M., Sukhbold T., 2018, MNRAS, 475, 2659
Marino R. A. et al., 2013, A&A, 559, A114
Mattila S. et al., 2016, The Astronomer's Telegram, 8992, 1
Mazzali P. A., Sullivan M., Pian E., Greiner J., Kann D. A., 2016, MNRAS, 458, 3455
McGaugh S. S., 1991, ApJ, 380, 140
Metzger B. D., Vurm I., Hascoët R., Beloborodov A. M., 2014, MNRAS, 437, 703
Minkowski R., 1941, PASP, 53, 224
Modjaz M., Gutiérrez C. P., Arcavi I., 2019, Nat. Astron., 3, 717
Moriya T. J., Tominaga N., 2012, ApJ, 747, 118
Moriya T. J., Sorokina E. I., Chevalier R. A., 2018, Space Sci. Rev., 214, 59
Müller T., Prieto J. L., Pejcha O., Clocchiatti A., 2017, ApJ, 841, 127
Nadyozhin D. K., 1994, ApJS, 92, 527
Nicholl M. et al., 2014, MNRAS, 444, 2096
Nicholl M. et al., 2015a, MNRAS, 452, 3869
Nicholl M. et al., 2015b, ApJ, 807, L18
Nicholl M. et al., 2016, ApJ, 826, 39
Nicholl M. et al., 2020, Nat. Astron., 4, 893
Nicholl M., Berger E., Margutti R., Blanchard P. K., Milisavljevic D., Challis P., Metzger B. D., Chornock R., 2017a, ApJ, 835, L8
Nicholl M., Guillochon J., Berger E., 2017b, ApJ, 850, 55
Nicholl M., Berger E., Blanchard P. K., Gomez S., Chornock R., 2019, ApJ, 871, 102
Ofek E. O. et al., 2014, ApJ, 781, 42
Pagel B. E. J., Edmunds M. G., Blackwell D. E., Chun M. S., Smith G., 1979, MNRAS, 189, 95
Parrag E. et al., 2021, MNRAS, 506, 4819
Pastorello A. et al., 2010, ApJ, 724, L16
Pastorello A. et al., 2021, Transient Name Server Classification Report, 2021–511, 1
Perley D. A. et al., 2015, ApJ, 801, 102
Pignata G. et al., 2004, MNRAS, 355, 178
Planck Collaboration XIII, 2016, A&A, 594, A13
Prentice S. J. et al., 2019, MNRAS, 485, 1559
Quimby R. M. et al., 2011, Nature, 474, 487
Rayner J. T., Toomey D. W., Onaka P. M., Denault A. J., Stahlberger W. E., Vacca W. D., Cushing M. C., Wang S., 2003, PASP, 115, 362
Renzo M., Farmer R., Justham S., Götberg Y., de Mink S. E., Zapartas E., Marchant P., Smith N., 2020, A&A, 640, A56
Richardson D., Jenkins R. L. I., Wright J., Maddox L., 2014, AJ, 147, 118
Riess A. G. et al., 1999, AJ, 118, 2675
Riess A. G., Casertano S., Yuan W., Bowers J. B., Macri L., Zinn J. C., Scolnic D., 2021, ApJ, 908, L6
Roy R. et al., 2016, A&A, 596, A67
Schlafly E. F., Finkbeiner D. P., 2011, ApJ, 737, 103
Schulze S. et al., 2018, MNRAS, 473, 1258
Skrutskie M. F. et al., 2006, AJ, 131, 1163
Smartt S. J. et al., 2015, A&A, 579, A40
Smartt S. J., 2009, ARA&A, 47, 63
Smith N. et al., 2007, ApJ, 666, 1116
Smith N. et al., 2015, MNRAS, 449, 1876
Smith M. et al., 2016, ApJ, 818, L8
Smith N., 2017, Interacting Supernovae: Types IIn and Ibn. Springer International Publishing, Cham, p. 403
Smith N., McCray R., 2007, ApJ, 671, L17
Soderberg A. M. et al., 2008, Nature, 453, 469
Soker N., Gilkis A., 2017, ApJ, 851, 95
Stevance H. F., Eldridge J. J., 2021, MNRAS, 504, L51
Stritzinger M. et al., 2002, AJ, 124, 2100
Tonry J. et al., 2018b, Transient Name Server Discovery Report, 2018–1680, 1
Tonry J. L. et al., 2012, ApJ, 750, 99
Tonry J. L. et al., 2018a, ApJ, 867, 105
van Dokkum P. G., 2001, PASP, 113, 1420
Villar V. A., Nicholl M., Berger E., 2018, ApJ, 869, 166
Vurm I., Metzger B. D., 2021, ApJ, 917, 77
Wang S. Q., Wang L. J., Dai Z. G., Wu X. F., 2015, ApJ, 799, 107
Weiler K., 2003, Supernovae and Gamma-Ray Bursters. Lecture Notes in Physics Vol. 598. Springer, Berlin, Heidelberg
Woosley S. E., 2010, ApJ, 719, L204
Woosley S. E., 2017, ApJ, 836, 244
Woosley S. E., Blinnikov S., Heger A., 2007, Nature, 450, 390
Yan L. et al., 2015, ApJ, 814, 108
Yan L. et al., 2017a, ApJ, 840, 57
Yan L. et al., 2017b, ApJ, 848, 6
Yang Y. et al., 2020, ApJ, 902, 46
Yaron O., Gal-Yam A., 2012, PASP, 124, 668
Zaritsky D., Kennicutt Robert C. J., Huchra J. P., 1994, ApJ, 420, 87
Zou Y.-C., Cheng K. S., 2018, Publ. Astron. Soc. Aust., 35, 32

SUPPORTING INFORMATION

Supplementary data are available at *MNRAS* online.

Please note: Oxford University Press is not responsible for the content or functionality of any supporting materials supplied by the authors. Any queries (other than missing material) should be directed to the corresponding author for the article.

APPENDIX A: TABLES

Table A1. *uvw*1-, *uvm*2-, *uvw*2-filter observed (non *K*-corrected) aperture magnitudes (in AB system). Errors are in parentheses. The full table is available online as supplementary material..

MJD	r. f. phase [d]	*uvw*2	*uvm*2	*uvw*1	Instrument
58430.65	− 31.89	20.17(0.12)	19.76(0.14)	18.90(0.09)	*Swift*/UVOT
58431.56	− 31.03	20.21(0.12)	19.73(0.12)	18.65(0.08)	*Swift*/UVOT
58434.92	− 27.87	19.92(0.11)	19.54(0.12)	18.47(0.08)	*Swift*/UVOT
58436.44	− 26.44	19.88(0.11)	19.37(0.11)	18.39(0.08)	*Swift*/UVOT
–	–	–	–	–	–

Table A2. *u*-, *g*-, *r*-, *i*-, *z*-filter observed (non *K*-corrected, non S-corrected) magnitudes (in AB system). Errors are in parentheses. The full table is available online as supplementary material.

MJD	r. f. phase [d]	*u*	*g*	*r*	*i*	*z*	Instrument
58413.54	− 48.01	–	–	19.31(0.16)	–	–	ATLAS
58423.53	− 38.60	–	–	18.54(0.19)	–	–	ATLAS
58424.54	− 37.65	–	–	18.51(0.14)	–	–	ATLAS
58426.12	− 36.16	–	18.05(0.01)	17.90(0.01)	17.76(0.02)	–	LCO+Sinistro
–	–	–	–	–	–	–	

Table A3. *U*-, *B*-, *V*-observed (non *K*-corrected, non S-corrected) magnitudes (in AB system). The full table is available online as supplementary material.

MJD	r. f. phase [d]	*U*	*B*	*V*	Instrument
58426.12	− 36.16	–	18.37(0.01)	17.90(0.02)	LCO+Sinistro
58427.15	− 35.19	–	18.09(0.02)	17.87(0.01)	LCO+Sinistro
58428.31	− 34.1	–	17.95(0.02)	17.69(0.01)	LCO+Sinistro
58429.29	− 33.17	–	17.83(0.04)	17.56(0.01)	LCO+Sinistro
–	–	–	–	–	–

Table A4. *J*-, *H*-, K_s-observed (non *K*-corrected) magnitudes (in AB system). Errors are in parentheses.

MJD	r. f. phase [d]	*J*	*H*	K_s	Instrument
58512.96	45.56	15.60(0.01)	15.91(0.01)	16.75(0.01)	NOT+NOTCam
58546.87	77.51	16.21(0.02)	16.36(0.02)	17.37(0.03)	NOT+NOTCam
58563.85	93.50	–	17.77(0.04)	17.89(0.04)	NOT+NOTCam

Table A5. *W*1-, *W*2-observed (non *K*-corrected) magnitudes (in AB system). Errors are in parentheses.

MJD	r. f. phase [d]	*W*1	*W*2	Instrument
58507.39	40.04	17.95(0.07)	18.33(0.13)	WISE
58712.64	233.69	19.13(0.16)	$\gtrsim$18.61	WISE

Table A6. S-corrections for Schmidt and AFOSC filters (Asiago observatory). The full table is available online as supplementary material.

MJD	*B*	*g*	*V*	*r*	*i*
58430.25	− 0.02	0.01	0.018	0.113	0.053
58437.02	− 0.019	0.014	0.022	0.122	0.048
58437.14	− 0.017	0.014	0.019	0.127	0.06
58440.23	− 0.027	0.012	0.018	0.101	0.064
–	–	–	–	–	–

Table A7. S-corrections for Sinistro (LCO). The full table is available online as supplementary material.

MJD	*B*	*g*	*V*	*r*	*i*
58430.25	− 0.009	0.003	0.009	0.004	− 0.005
58437.02	− 0.008	0.004	0.003	0.007	− 0.002
58437.14	− 0.008	0.005	0.011	0.005	− 0.001
58440.23	− 0.009	0.004	0.009	− 0.007	− 0.0
–	–	–	–	–	–

Table A8. S-corrections for NOT filters. The full table is available online as supplementary material.

MJD	*B*	*g*	*V*	*r*	*i*
58430.25	− 0.013	0.001	0.008	0.011	− 0.008
58437.02	− 0.013	− 0.004	0.005	0.013	− 0.011
58437.14	− 0.014	− 0.002	0.011	0.015	− 0.013
58440.23	− 0.015	− 0.005	0.007	0.002	0.011
–	–	–	–	–	–

Table A9. S-corrections for *Swift*/UVOT. The full table is available online as supplementary material.

MJD	*B*	*V*
58430.25	− 0.017	0.009
58437.02	− 0.018	0.008
58437.14	− 0.017	0.019
58440.23	− 0.02	0.006
–	–	–

Table A10. Estimated uncertainties $\Delta S_{\rm corr}$ for the filters *u*, *U*, *z*, *J*, *H*, $K_{\rm s}$ (for each instrument) divided in two temperature ranges (see the text). The full table is available online as supplementary material.

	5000 K < *T* < 10 000 K	10 000 K < *T* < 20 000 K
NOT+ALFOSC/NOTCam	$\Delta S_{{\rm corr},u} = 0.30$	$\Delta S_{{\rm corr},u} = 0.20$
	$\Delta S_{{\rm corr},z} = 0.03$	$\Delta S_{{\rm corr},z} = 0.01$
	–	–
–	–	–

Table A11. *K*-corrections expressed in magnitudes. The full table is available online as supplementary material.

Rest-frame phase [d]	*uvw*2 filter	*uvm*2 filter	*uvw*1 filter	*u* filter	*U* filter	*B* filter	*g* filter	*V* filter	*r* filter	*i* filter	*z* filter	*J* filter	*H* filter	$K_{\rm s}$ filter
−32.36	− 0.106	− 0.098	0.031	0.191	0.191	0.009	− 0.008	0.030	− 0.002	0.043	− 0.206	− 0.154	− 0.030	0.402
−25.98	− 0.100	− 0.103	0.037	0.166	0.173	− 0.015	− 0.022	0.028	0.004	0.068	− 0.203	− 0.159	− 0.030	0.148
−25.87	− 0.102	− 0.105	0.037	0.165	0.173	− 0.011	− 0.016	0.038	0.005	0.131	− 0.203	− 0.159	− 0.030	0.146
−22.96	− 0.083	− 0.055	0.080	0.129	0.137	− 0.020	− 0.023	0.028	0.013	− 0.012	− 0.202	− 0.147	− 0.033	0.089
–	–	–	–	–	–	–	–	–	–	–	–	–	–	–

Table A12. Logarithm of the bolometric luminosities integrated over the *uvw*2, *uvm*2, *uvw*1, *U*, *B*, *g*, *V*, *r*, *i*, *z*, *J*, *H*, $K_{\rm s}$, *W*1, *W*2 filters. The full table is available online as supplementary material.

Rest-frame phase [d]	$\log_{10} L_{\rm bol}$
−48.01	43.30(0.04)
−38.60	43.61(0.04)
−37.65	43.62(0.04)
−36.16	43.86(0.04)
—	–

Table A13. Spectra in Fig. 5. The full table is available online as supplementary material.

MJD	Rest-frame phase [d]	Instrumental set-up [grism/grating]	Resolution [Å]
58428.57	− 34	LCO+FLOYDS	15.5
58429.57	− 33	LCO+FLOYDS	15
58430.25	− 32	NTT+EFOSC2 [gr13]	18
58433.19	− 29	HET+LRS2	–
–	–	–	–

Note. (*)This spectrum was not included in Fig. 5 because of its poor signal-to-noise ratio, but it will be made available within the online data set (see the Data Availability statement).

[1]*European Centre for Theoretical Studies in Nuclear Physics and Related Areas (ECT*), Fondazione Bruno Kessler, Trento, Italy*
[2]*INAF - Osservatorio Astronomico di Padova, Vicolo dell'Osservatorio 5, I-35122 Padova, Italy*
[3]*Birmingham Institute for Gravitational Wave Astronomy and School of Physics and Astronomy, University of Birmingham, Birmingham B15 2TT, UK*
[4]*Institute for Astronomy, University of Edinburgh, Royal Observatory, Blackford Hill, Edinburgh EH9 3HJ, UK*
[5]*Departamento de Ciencias Físicas - Universidad Andres Bello, Avda. República 252, Santiago 8320000, Chile*
[6]*Millennium Institute of Astrophysics, Nuncio Monsenor Sótero Sanz 100, Providencia, Santiago, Chile*
[7]*INAF - Osservatorio Astronomico di Brera, Via Bianchi 46, I-23807 Merate, Italy*
[8]*Department of Astronomy, The Ohio State University, 140 W. 18th Avenue, Columbus, OH 43210, USA*
[9]*Center for Cosmology and AstroParticle Physics (CCAPP), The Ohio State University, 191 W.Woodruff Avenue, Columbus, OH 43210, USA*
[10]*IAASARS, National Observatory of Athens, 15236 Penteli, Greece*
[11]*Department of Astrophysics, Astronomy & Mechanics, Faculty of Physics, National and Kapodistrian University of Athens, 15784 Athens, Greece*
[12]*Nordic Optical Telescope, Apartado 474, E-38700 Santa Cruz de La Palma, Santa Cruz de Tenerife, Spain*
[13]*Department of Physics and Astronomy, Aarhus University, NyMunkegade 120, DK-8000 Aarhus C, Denmark*
[14]*Center for Astrophysics | Harvard & Smithsonian, 60 Garden Street, Cambridge, MA 02138-1516, USA*
[15]*School of Physics and Astronomy, University of Southampton, Southampton, Hampshire SO17 1BJ, UK*
[16]*Las Cumbres Observatory, 6740 Cortona Dr. Suite 102, Goleta, CA 93117, USA*
[17]*Department of Physics, University of California, Santa Barbara, Santa Barbara, CA 93106, USA*
[18]*Physics Department and Tsinghua Center for Astrophysics (THCA), Tsinghua University, Beijing 100084, China*
[19]*The Oskar Klein Centre, Department of Astronomy, Stockholm University, AlbaNova, SE-10691 Stockholm, Sweden*
[20]*Kavli Institute for Astronomy and Astrophysics, Peking University, Yi He Huan Road 5, Hai Dian District, Beijing 100871, China*
[21]*INFN – Sezione di Padova, Via Francesco Marzolo 8, I-35131 Padova, Italy*
[22]*Space Telescope Science Institute, 3700 San Martin Drive, Baltimore, MD 21218, USA*
[23]*Astronomical Observatory, University of Warsaw, Al. Ujazdowskie 4, PL-00-478 Warszawa, Poland*
[24]*Finnish Centre for Astronomy with ESO (FINCA), University of Turku, FI-20014 Turku, Finland*
[25]*Tuorla Observatory, Department of Physics and Astronomy, University of Turku, FI-20014 Turku, Finland*
[26]*Center for Astrophysics | Harvard & Smithsonian, 60 Garden Street, Cambridge, MA 02138-1516, USA*
[27]*The NSF AI Institute for Artificial Intelligence and Fundamental Interactions*
[28]*Steward Observatory, University of Arizona, 933 North Cherry Avenue, Tucson, AZ 85721-0065, USA*
[29]*Department of Physics and Astronomy, University of Turku, FI-20014 Turku, Finland*
[30]*Max-Planck-Institut für Astrophysik, Karl-Schwarzschild-Str 1, D-85748 Garching, Germany*
[31]*School of Physics, Trinity College Dublin, The University of Dublin, Dublin 2, Ireland*
[32]*Dipartimento di Fisica e Astronomia G. Galilei, Universitá di Padova, Vicolo dell'Osservatorio 3, I-35122 Padova, Italy*
[33]*Post Astronomy, Lexington, MA 02421, USA*
[34]*Institute of Space Sciences (ICE, CSIC), Campus UAB, Carrer de Can Magrans s/n, E-08193 Barcelona, Spain*
[35]*Department of Physics, Florida State University, 77 Chieftan Way, Tallahassee, FL 32306, USA*
[36]*Physik Department, Technische Universität München, James-Franck Str 1, D-85748 Garching, Germany*
[37]*Department of Astronomy, University of Texas at Austin, 2515 Speedway, Stop C1400, Austin, TX 78712-1205, USA*
[38]*Konkoly Observatory, CSFK, Konkoly-Thege M. út 15-17, Budapest 1121, Hungary*
[39]*Institute of Physics, ELTE Eötvös Loránd University, Pázmány Péter sétány 1/A, Budapest 1117 Hungary*
[40]*Department of Optics & Quantum Electronics, University of Szeged, Dóm tér 9, Szeged 6720, Hungary*
[41]*Astrophysics Research Centre, School of Mathematics and Physics, Queen's University Belfast, Belfast BT7 1NN, UK*

This paper has been typeset from a TEX/LATEX file prepared by the author.